Fabrication and Optimal Strain Sensor Placement in an Instrumented Disk Drive Suspension for Vibration Suppression

Kenn Oldham, Stanley Kon
Computer Mechanics Laboratory (CML)
University of California at Berkeley, CA
94720-1740
oldham, kon@me.berkeley.edu

Roberto Horowitz Faculty of Mechanical Engineering
University of California at Berkeley, CA
94720-1740
horowitz@me.berkeley.edu

October 27, 2003

Abstract

Instrumenting a disk drive suspension with vibration sensing strain gages can enhance vibration suppression in hard disk drives, provided that the gages are properly located and sufficiently sensitive. The cost function of an optimal LQG controller with Kalman filter is proposed as an objective function for determining the optimal location and orientation of displacement sensors on a flexible structure, such as strain gages on a disk drive suspension. Analytical bounds are derived for the Kalman filter Riccati equation in a modal system with large sensor noise. These bounds produce analytical approximations that reduce the computational complexity of the LQG optimization approach with cheap control. Results are applied to a prototype disk drive suspension to identify sensor positions and sensor requirements. Piezoresistive and piezoelectric thin films are discussed as materials for meeting these requirements in an instrumented suspension. The performance of prototype sensors installed using MEMS-style processing techniques on stainless steel wafers is examined.

1 Introduction

Increasing data storage densities in computer hard disk drives require positioning drives' read-write heads over ever-smaller data bits. As the industry targets bit densities of 1 terabit per square inch, airflow induced vibration of the mechanical servo assembly becomes a major obstacle to attaining the necessary servo precision. In particular, excitation of vibration modes in the e-block and suspension upon which the head and air bearing are mounted will cause significant off-track error during tracking operations.

One method of improving servo capabilities to overcome these problems is to incorporate a second actuator into the servo

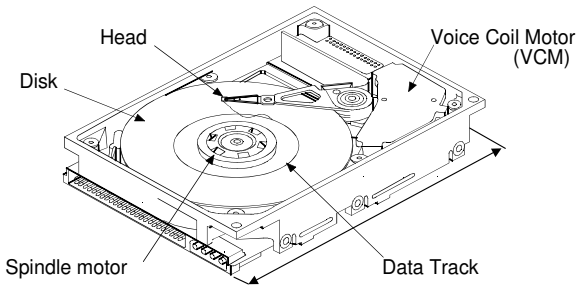

Figure 1: Conventional disk drive configuration

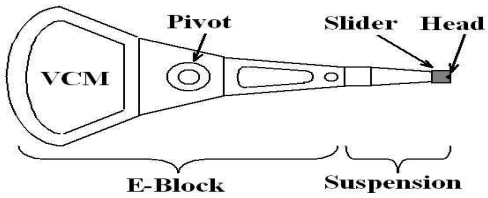

Figure 2: Conventional disk drive servo assembly

system. Currently, disk drives rely on a single large voice-coil motor for actuation (see Fig. 1 and 2). Proposed dual-stage configurations include actuated suspensions (Fig. 3a), with a microactuator built into the suspension itself, and actuated sliders (Fig. 3b) and heads, with smaller microactuators installed underneath or inside the slider, beyond the vibrating region. In either case, the smaller second actuator is able to operate at a higher bandwidth than the conventional voice-coil motor (VCM), and thus damp out higher frequency vibration modes.

Several researchers have examined the use of additional sensors within a disk drive to better detect and reject vibration disturbances. Adding sensors to the disk drive permits acquisition of vibration information at a higher sampling rate and closer to the point of disturbance than is possible from position error signals taken from the disk itself. This information may be fed back to the VCM or actuated slider or fed forward to actuated sliders and heads. In one study, simulation of a single stage system predicted a 500 Hz bandwidth improvement from placing a single stain sensor on a suspension [1] to detect resonant suspension modes. In one experimental test, a strain sensor mounted on the suspension e-block was used to damp out the e-block butterfly mode [2], while in another test, a PZT actuated slide was split for sensing and actuating purposes and used to damp both butterfly and suspension sway modes [3].

In designing a strain gage for vibration detection on a disk drive suspension, it is important to place the gage in a location

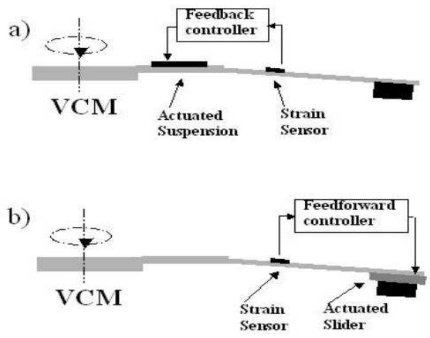

Figure 3: Dual-stage disk drive servo configurations

that provides the maximum amount of useful information to the servo system controller. Not only should a strong signal be available, but it should include any vibration modes that could contribute to off-track error at the read-write head should be visible. However, vibration modes that do not cause off-track error should be avoided, as the signal from these modes will unnecessarily excite the controller.

Micro-scale processing techniques allow precise installation of vibration sensors at locations that meet these demands. Lithographic patterning permits definition of small, focused sensors at locations judged to be optimal. Certain semiconductor and thin film processing techniques may also produce higher sensitivity gages than conventional methods, and may be integrated into fabrication and assembly of a disk drive servo system.

In general terms, finding optimal strain gage locations is a problem of optimal placement of an arbitrary number of displacement sensors on a flexible structure. Hac and Liu [4] applied an observability criteria to this problem, which was adapted to disk drives by Banther, et al. [5] and Gross [6]. However, while this criterion ensures that all modes are visible, the resulting sensor locations may not be optimal when incorporated into a feedback control system. Several researchers have proposed using some objective function based on Kalman filter results [7] [**?**] and Kondoh et al. [9] incorporated controller structure by minimizing the quadratic cost function in standard LQ optimal control. Solution of the standard LQ problem does provide an optimal result in terms of the H2 norm of the system, but the approach is computationally intensive and requires knowledge about the stochastic properties of the system.

In this paper, we optimize sensor locations on a disk drive suspension according to the cost function of the standard LQ problem, but present numerical approximations of the Riccati equation solutions to simplify the computational complexity and relax requirements on knowledge about the stochastic system. We then explore several methods of fabricating strain gage vibration sensors on a disk drive suspension and give experimental results for several combinations of materials and processing

techniques.

2 Sensor Location

The disk drive servo system described here consists of the flexible suspension with inputs from the voice coil motor (VCM) and airflow disturbances, plus an actuated-slider microactuator at the tip of the suspension. The motion of a flexible structure can be written as the summation of modal contributions. For instance, off-track displacement, z, of the read-write head may be written as

$$z = \sum_{i=1}^{n} d_i \nu_i + x_{MA} \tag{1}$$

where ν_i is a modal coordinate for mode i, x_{MA} is the displacement of the microactuator relative to the tip of the suspension, d_i is the displacement at the tip of the suspension in the modal coordinate for mode shape i, and n is the number of modes considered.

Similarly, strain gage measurements from this system are

$$y_k = \sum_{i=1}^{n} c_{ki} \nu_i \qquad c_{ki} = K_{sense} c'_{ki} \tag{2}$$

where y_k is the strain gage output voltage and c_{ki} is the magnitude of strain, ϵ at the sensor location resulting from mode i, c'_{ki}, times the sensor gain, K_{sense} in V/ϵ.

The modal dynamics are driven both by the VCM and disturbances:

$$\ddot{\nu_i} + 2\xi_i \omega_i \dot{\nu_i} + \omega_i^2 \nu_i = \sum_{k=1}^{l} b_{ik} \omega_i^2 w_k + \omega_i^2 u_{VCM} \tag{3}$$

.

Here, the dynamics of each mode are described by its natural frequency, ω_i, and damping ration, ξ_i. The modal coordinates are normalized to ω_i^2 times the VCM input for convenience in later manipulation. The b_{ik} coefficients adjust disturbance k for its influence relative to the VCM on mode i, due to differeing location and frequency weighting.

The microactuator dynamics have a similar description,

$$\ddot{x}_{MA} + 2\xi_{MA}\omega_{MA}\dot{x}_{MA} + \omega_{MA}^2 x_{MA} = K_{MA} u_{MA} \tag{4}$$

with ω_{MA} and ξ_{MA} the natural frequency and damping ratio of the microactuator, and K_{MA} the microactuator gain.

In state space, the system may be described in the form

$$\dot{x} = Ax + Bu + B_w w \tag{5}$$

$$y = Cx + v \tag{6}$$

$$z = Dx \tag{7}$$

$$E[w^T w] = \mathrm{w} I_{l\times l} \qquad E[v^T v] = \mathrm{v} I_{r\times r} \tag{8}$$

As before, $z \in \mathbb{R}$ is the off-track error at the slider and $y \in \mathbb{R}^{r+1}$ is the output from r strain gages plus an additional measurement of relative position error signal (RPES) measured by the microactuator. The inputs are l white disturbances in $w \in \mathbb{R}^l$ with spectral density w and two actuated inputs, from the VCM and microactuator, included in $u \in \mathbb{R}^2$. Sensor noise is $v \in \mathbb{R}^r$, white with spectral density v. A number of experimental results have verified that airflow excitation has broadband frequency spectrum and can be accurately modelled by zero-mean input white noise [10] [11].

The state vector $x \in \mathbb{R}^{2n+2}$ consist of the modal and microactuator coordinate displacements and normalized velocities,

$$x_{2i-1} = \nu_i \qquad x_{2i} = \frac{\dot{\nu_i}}{\omega_i} \tag{9}$$

$$x_{2N+1} = x_{MA} \qquad x_{2N+2} = \frac{\dot{x}_{MA}}{\omega_{MA}} \tag{10}$$

The state matrices are

$$A = \begin{bmatrix} A_1 & 0 & \cdots & & 0 \\ 0 & A_2 & & & \vdots \\ \vdots & & \ddots & & \\ & & & A_n & 0 \\ 0 & \cdots & & 0 & A_{MA} \end{bmatrix} \tag{11}$$

$$A_i = \begin{bmatrix} 0 & \omega_i \\ -\omega_i & -2\xi_i\omega_i \end{bmatrix} \qquad A_{MA} = \begin{bmatrix} 0 & \omega_{MA} \\ -\omega_{MA} & -2\xi_{MA}\omega_{MA} \end{bmatrix} \tag{12}$$

$$B = \begin{bmatrix} 0 & 0 \\ 0 & \omega_1 \\ 0 & 0 \\ 0 & \omega_2 \\ \vdots & \vdots \\ 0 & 0 \\ 0 & \omega_n \\ 0 & 0 \\ K_{MA}\omega_{MA} & 0 \end{bmatrix} \qquad B_w = \begin{bmatrix} 0 & \cdots & 0 \\ b_{11}\omega_1 & \cdots & b_{1l}\omega_1 \\ 0 & \cdots & 0 \\ b_{21}\omega_2 & \cdots & b_{2l}\omega_2 \\ \vdots & & \vdots \\ 0 & \cdots & 0 \\ b_{n1}\omega_n & \cdots & b_{nl}\omega_n \\ 0 & \cdots & 0 \\ 0 & \cdots & 0 \end{bmatrix} \tag{13}$$

$$C(\Phi) = \begin{bmatrix} c_{11}(\Phi_1) & 0 & c_{12}(\Phi_1) & 0 & \cdots & c_{1n}(\Phi_1) & 0 & 0 & 0 \\ \vdots & \vdots & \vdots & \vdots & & \vdots & \vdots & & \\ c_{r1}(\Phi_r) & 0 & c_{r2}(\Phi_r) & 0 & \cdots & c_{rn}(\Phi_r) & 0 & 0 & 0 \\ 0 & 0 & 0 & 0 & \cdots & 0 & 0 & c_{es} & 0 \end{bmatrix} \tag{14}$$

$$D = \begin{bmatrix} d_1 & 0 & d_2 & 0 & \cdots & d_n & 0 & 1 & 0 \end{bmatrix} \tag{15}$$

b_{ij} and d_i are defined as before, while $c_{ij}(\Phi_j)$ is the strain from mode j measured at strain gage i, written explicitly as function of the location and orientation, Φ_i, of the sensor. c_{es} is the RPES signal gain from the microactuator.

2.1 Optimization Theory

Our objective is to choose a sensor location and orientation that minimizes off-track error of the closed-loop system. We choose to minimize the H2 norm of the system when implementing the optimal linear quadratic gaussian, or LQG, controller and filter.

$$\min_{\Phi} J_{H2} = \min_{\Phi} \left\{ \min_{K,F(\Phi)} E\left[\int_0^\infty z^T z + u^T R u dt \right] \right\} \tag{16}$$

with K the optimal linear, stationary controller, $F(\Phi)$ the optimal linear, stationary filter for a given $C(\Phi)$, and R a weighting function on the inputs. Vector Φ includes all coordinates and orientations of sensors that may be varied during optimization.

K and F are obtained by solving Riccati equations. The linear controller, K, for this system is not dependant on sensor location:

$$u = -K\hat{x} \tag{17}$$

$$K = R^{-1}B^T P \tag{18}$$

$$A^T P + PA - PBR^{-1}B^T P + D^T D = 0 \tag{19}$$

The optimal linear filter, F, is a Kalman filter and does depend on sensor location

$$\dot{\hat{x}} = A\hat{x} + Bu + MC(\Phi)^T \mathrm{v}^{-1}\left[\hat{y} - C(\Phi)\hat{x}\right] \tag{20}$$

$$F = MC(\Phi)^T \mathrm{v}^{-1} \tag{21}$$

$$AM + MA^T - MC(\Phi)^T \mathrm{v}^{-1} C(\Phi) M + B_w \mathrm{w} B_w^T = 0 \tag{22}$$

The value of the objective function with this controller and filter is

$$J_{H2} = tr\left[PK\mathrm{v}K^T + MD^T D\right]. \tag{23}$$

Since the range of motion of both the VCM and microactuator is very large relative to suspension vibration, we solve the above equations for the case of cheap control, $R \to 0$. From loop transfer recovery (LTR) results [14], in this situation $P \to 0$ and

$$J_{H2} \to tr\left[MD^T D\right] = \sum_i \sum_j m_{2i-1,2j-1} d_i d_j. \tag{24}$$

The drawbacks of this optimization method are requirements on knowledge about the system and computational complexity. Reasonable results require reliable estimates of disturbance and noise magnitudes. Even when this information is available, solving the Riccati equation at many locations requires a large amount of computation time. In the following section, we derive an approximation for the Riccati equation in a system described by the modal components described previously.

An alternative to LQG optimization is to optimize some measure of the observability of the system. The observability gramian for a state space system is

$$Q = \int_0^\infty y^T(t)y(t)\mathrm{d}t, \tag{25}$$

which for asympotically stable systems satisfies

$$A^T Q + QA + C(\Phi)^T C(\Phi) = 0. \tag{26}$$

The eigenvalues of the observability gramian are a measure of the energy from each mode for a given sensor placement, and can thus be used as a basis for locating sensors. Various objective functions based on eigenvalues of the observability gramian have been proposed, as in [5] and [4]. However, as will be discussed later, observability approaches may neglect the relative importance of the modes in causing off-track error, and not necessarily provide the best signal in a closed-loop system.

2.2 Approximate Riccati Solution

While an exact analytical solution to the Riccati equation exists, it requires a large number of calculations and can make optimization impractical, especially for a large numbers of variables. A 2n-eigenvalue problem must be solved to obtain the estimation error covariance matrix M at each location Φ. Observability-based approaches are also relatively complex, requiring solution of an n-eigenvalue problem. This makes sensor optimization difficult for systems with large numbers of modes or many potential sensor locations.

To mitigate this problem, we have derived a set of approximations for the terms of M that appear in the objective function under cheap control, as shown in (46). For a system with the state space form above, bounds may be placed on certain terms of matrix M, including all those which appear in objective function (46). Under certain conditions, these bounds approximate the values of the diagonal terms in M and show them to be much larger than the off-diagonal terms. The full derivation of the approximations is included in the appendix.

The chief approximation result is that if for all i and j,

1. Modes are widely spaced:

$$|\omega_i - \omega_j| \gg 0 \tag{27}$$

2. Sensor noise is large relative to other parameters:

$$|c_{ji}| \left(\sum_{k=1}^{l} |b_{ik}| \right) \frac{\mathrm{w}}{\mathrm{v}} \ll 1 \tag{28}$$

then, for all i, in an undamped system

$$m_{2i-1,2i-1} \approx \frac{\sqrt{\sum_{p=1}^{l} b_{ip}^2}\omega_i \sqrt{\mathrm{wv}}}{\sqrt{\sum_{k=1}^{r} c_{ki}^2}} \tag{29}$$

and in a lightly damped system

$$m_{2i-1,2i-1} \approx \frac{-4\xi_i\omega_i + \sqrt{(4\xi_i\omega_i)^2 + \frac{4\omega_i^2 \mathrm{w}}{\mathrm{v}} \left(\sum_{k=1}^{r} c_{ki}^2\right) \left(\sum_{p=1}^{l} b_{ip}^2\right)}}{\frac{2}{\mathrm{v}} \sum_{k=1}^{r} c_{ki}^2} \tag{30}$$

.

Furthermore, in both cases, for all i and j,

$$m_{2i-1,2i-1} \gg m_{2i-1,2j-1}. \tag{31}$$

Therefore, the objective function for low cost control can be approximated as

$$J_{H2} \approx \sum_{i=1}^{n} d_i^2 m_{2i-1,2i-1} \tag{32}$$

given by (29) or (30). This result is also true for a discrete time system derived from the continuous time model described above, under the same conditions and with high sampling frequency.

Approximating the objective function in this manner has several advantages. Its main effect is that it greatly simplifies the computation of the objective function. It reduces the problem of solving for n eigenvalues to a straightforward algebraic computation. This is especially useful for a system with many modes or sensor location variables. However, the approximate solution also provides insight into the physical trade-offs between parameters of the system, and reduces the amount of knowledge needed about the system beforehand.

First, we comment on the conditions under which the approximation holds. Widely-spaced modes are a common requirement for simple analysis of modal systems. More interesting is the second condition, (28), which indicates that the approximation applies to systems with large sensor noise. In fact, it seems to imply that the signal from the sensors will be below the noise floor of the system, but the addition of multiple modes and the presence of resonant peaks can raise the signal well above the noise floor while (28) remains satisfied. Furthermore, many of the bounds used to derive the approximation are loose, so that the approximation may be reasonable even for smaller noise levels. However, the approximation should be checked against the exact solution for several test cases if this is attempted.

When the approximation does perform well, the relative significance of the parameters in the system model is visible, which can be useful for design and interpretation; a criticism of the use of Kalman filter methods for optimizing sensor locations is lack of a physical interpretation of the result. The best sensor locations will have large strains, or in other words large c_{ki} coefficients, as one would expect. However, in a choosing between strain contributions from different modes when there is a trade-off, a more optimal location will emphasize the mode with a larger contribution to off-track error, as computed from the sum of input coefficients to that mode, the b_{ip}'s, and the modal displacement coefficient at the slider, d_i. Adding damping to the system diminishes the difference between modal contributions.

We can compare our proposed method to the observability methods. For a lightly-damped system, the eigenvalues of the observability grammian can be approximated as

$$\lambda_{2i-1}, \lambda_{2i} \approx \frac{\sum_{k=1}^{r} c_{ki}^2}{4\xi_i\omega_i}. \tag{33}$$

Maximizing the minimum eigenvalue is equivalent to minimizing the maximum inverse eigenvalue, or,

$$J_{opt} = \min_{C(\Phi)} \left[\max_i \left\{ \frac{4\xi_i \omega_i}{\sum_{k=1}^{r} c_{ki}^2} \right\} \right]. \tag{34}$$

The value to be minimized in the observability case is qualitatively similar to the LQG filter result, but the relative importance of each mode to off-track error is lacking. As a result, the observability approach will locate sensors so as to best detect modes with small strain contributions, ignoring more easily detected modes. If one of these modes causes proportionally larger off-track error than strain signal, it may be lost by the sensor at levels that cause significant off-track error. One solution, used in [[6]], is to weight the eigenvalues by their modal contribution to off-track error. This tends to give close agreement with LQG results, though it still neglects input coefficients and requires more computation.

Finally, the approximate solution shows that, for a noisy system, the optimal sensor location is independent of the exact noise and disturbance strength. Each of the diagonal terms in M is multiplied by the same $\sqrt{(}\mathrm{wv})$ constant. This means that only enough knowledge about the stochastic properties of the system to validate the approximate solution is required. The exact noise and disturbance levels need not be known prior to design of the system.

3 Optimization Results for Disk Drive Suspension

3.1 Optimization Implementation

A Hutchinson Technology, Inc. (HTI) 3430 suspension was modelled in ANSYS for finite element analysis of vibration modes. A modal analysis was performed to identify the natural frequencies of vibration, followed by a harmonic analysis near those frequencies to obtain the frequency response of the structure. The analysis provided transfer functions from VCM input to off-track displacement and to x-normal, y-normal, and xy-shear components of strain at any model element.

$$\frac{Z(s)}{U(s)} = \sum_{i=1}^{n} \frac{d_i \omega_i}{s^2 + 2\xi_i \omega_i s + \omega_i^2} \tag{35}$$

$$\frac{Y_k(s)}{U(s)} = \sum_{i=1}^{n} \frac{c'_{ki} \omega_i}{s^2 + 2\xi_i \omega_i s + \omega_i^2} \tag{36}$$

$$\tag{37}$$

Here, $U(s)$ is the VCM input in the frequency domain, $Z(s)$ is the frequency response of off-track error, and $Y_k(s)$ is the component of strain at sensor k from any single strain direction. Damping ratios, modal weights, and gains giving d_i and c'_{ki} were obtained via the circle fit method for modal identification.

The x-, y-, and xy- components of strain at each element were projected to a voltage output for an arbitrary strain gage orientation θ using Mohr's equation and the estimated gage sensitivity K_{sense},

Table 1: System Model Parameters

Variable	Units	Value
w	mN^2	1×10^{-7}
v	V^2	1×10^{-15}
K_{sense}	V/ϵ	60
$b_{11} : b_{41}$		1
b_{51}		0.5
b_{61}		0.1

$$C = K_{sense} \begin{bmatrix} \frac{1+\cos 2\theta}{2} & \frac{1-\cos 2\theta}{2} & \frac{\sin 2\theta}{2} \end{bmatrix} \begin{bmatrix} C_{\mathrm{x}} \\ C_{\mathrm{y}} \\ C_{\mathrm{xy}} \end{bmatrix}, \tag{38}$$

where C_{x}, C_{y}, and C_{xy} are the sensor output coefficients for the three strain components.

Stochastic parameters of the system (w,v) are estimated from strain gain models and experimental measurements of suspension vibration in other disk drives. We use a single disturbance and set input coefficients b_{11} to b_{41} equal to one, and reduce b_{51} and b_{61} to 0.5 and 0.1, respectively to reflect lower windage measurements at frequencies above 10 kHz. A more accurate model would include adjustments to all b_i's to match both spatial and frequency domain properties of the input disturbance, but this information is not well known. Table 1 lists the major optimization parameters to be specified.

Because the microactuator mode is uncoupled with the rest of the servo system in our model, we neglect it during sensor optimization. In reality, there may be some coupling between suspension vibration and microactuator displacement and correlation between disturbances to the suspension and microactuator. This could provide additional information about suspension vibration and thus influence sensor selection, but we choose not to assume that this information will be available.

3.2 Location Optimization Results

We evaluated the LQG cost function at 100 high-strain elements in the hinge region of the HTI 3430 suspension at sensor orientations from 0 to 180 degrees. The cost function was evaluated for both the exact solution for the Kalman filter Riccati equation and for the approximate solution discussed above. Fig. 4 shows the full ANSYS model of the suspension with the hinge regions highlighted. Fig. 5a and 5b show the 20 best elements for strain gage installation using both evaluations. Both the exact solution and the approximation identify element 1346 as optimal, with the strain gage oriented at 11 degrees for the exact solution and 10 degrees for the approximation.

The dynamic response from disturbance to sensor output and off-track error is shown in Fig. 6. The best sensor location

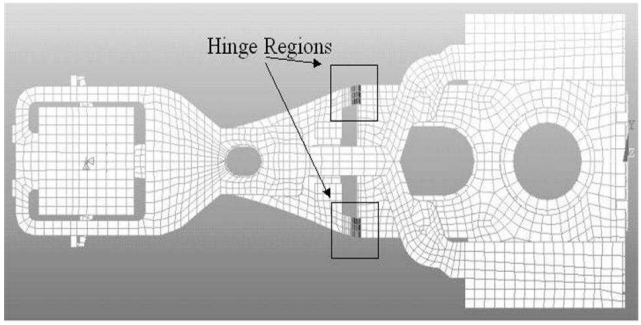

Figure 4: Ansys model of 3430 suspension

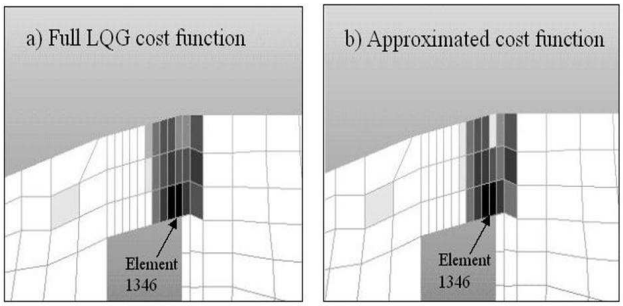

Figure 5: Optimal sensor locations (dark to light)

will have both a high level of strain and a large ratio of strain to off-track response at each mode. This results in a position that approximately matches the importance of modes at the sensor to their importance to off-track error at the slider. For this sensor location, the most difficult mode to detect is mode 5, a torsion mode, for which a disturbance producing one nanometer off-track displacement would produce 56 nanostrain at the sensor.

It is also clear from Fig. 5 that the approximate solution to the LQG cost function gives results that are very similar to the exact solution. This agreement can also be seen a individual sensor locations as a function of orientation. Fig. 7 plots the cost function as a function of angle for optimal element 1346. Both methods show undesirable orientations at 75 and 122 degrees,

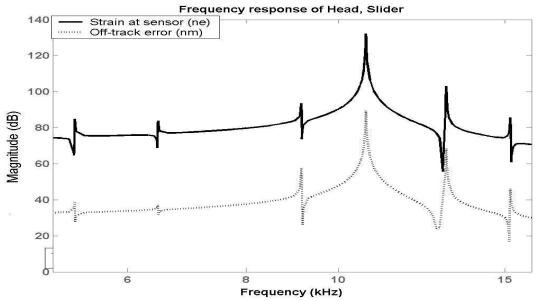

Figure 6: Frequency response of sensors and off-track disturbance

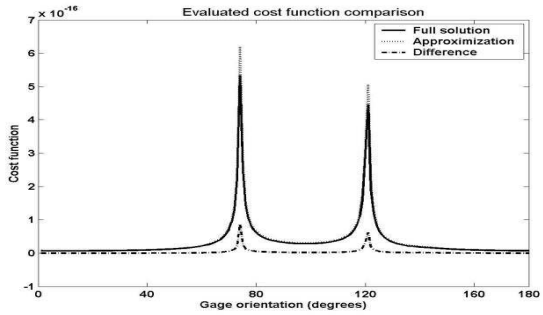

Figure 7: Cost function by sensor orientation, element 1346

Table 2: Comparison of exact and approximate Riccati solution

Mode i	ω_i (Hz)	$m_{2i-1,2i-1}$	Approximation	Error
1	5275	1.27	1.38	7.9%
2	6457	1.58	1.78	12.7%
3	9144	1.12	1.49	33.3%
4	10698	0.0271	0.0274	1.1%
5	5275	0.208	0.215	3.5%
6	5275	0.0368	0.0385	4.6%

and close agreement elsewhere.

The approximation we have developed is applicable to this situation because the strain in the system is very small, ranging from 10 to 100s of nanostrain for the level of disturbance anticipated. This results in very small c_{ki} coefficients that help satisfy (28). The largest value for a quantity in (28) is 0.16, large enough to cause some discrepancy between exact and approximate Riccati solutions, but still giving generally good agreement. Table 2 is an example of this: while the error between estimated and exact diagonal coefficients is as high as 33%, this is a small discrepancy for a set of diagonal terms of M that range over 3 orders of magnitude. Additionally and as expected, the largest off-diagonal term is much smaller, at $m_{7,9} = 1.7 \times 10^{-8}$.

4 Piezoresistive Sensors

To capitalize on identification of optimal sensor locations, a procedure for fabricating a strain gage precisely at those locations is required. We want to detect nanometer off-track error contribution from each mode; from our optimization of location, this corresponds to 56 nanostrain resolution at the sensor. Lithographically patterned piezoresistors are a common MEMS structure used to detect strain. Piezoelectric materials are also stain sensitive, and have also been used to form micro-scale devices. In this section we define the requirements on a piezoresistive or piezoelectric strain sensor based on the optimization results above.

4.1 Theory

The primary limitations on a piezoresistive strain gage are bias of the sensor resulting from temperature changes and intrinsic thermal noise in the sensor resulting from the resistivity of the sensor itself. The temperature dependence of the sensor may be greatly reduced by placing the sensor in a wheatstone bridge configuration. In our case, we assume a wheatstone bridge configuration with two opposing piezoresistors. The sensitivity of a strain gage to strain ϵ in this configuration can be calculated from

$$S = \frac{V_o}{\epsilon} = \frac{KV_i}{2} \tag{39}$$

where V_i is the input voltage to the bridge, V_o is the output voltage, and K is the gage factor of the piezoelectric material used in the sensor. Meanwhile, the thermal noise in the piezoresistor is

$$V_n = \sqrt{4kTRB} \tag{40}$$

where k is Boltzmann's constant, T is the temperature in Kelvin, R is the resistance of the gage, and B is the bandwidth being observed. The resolution, r of the bridge is given by

$$r = \frac{S}{V_n} \tag{41}$$

Table 3 shows estimates for various sensor materials. For these estimates, we assume a gage length of 100 μm to match our FEA model element size, a minimum length to width (L/W) ratio of 5 to limit the influence of longitudinal gage factor, and a minimum resistance of 200 Ω to ensure that gage resistance is at least 10 times higher than interconnect resistance. For this example, the sensor bandwidth is 20 kHz and the operating temperature is 300 K. We estimate input noise at the electronics to be 5 nV/$\sqrt{Hz}$.

Here, Constanten is a conventional metal strain gage material, SCS is p-type single crystal silicon [15], p-poly is p-type as referenced in [16], n-poly is n-type polysilicon (tested in U.C.Berkeley Microlab), and α-Si:H is hydrogenated amorphous silicon, first studied for its piezoresistive properties in [19].

From the table, we see that to detect strain in the 10^{-8} range with a piezoresistive sensor, a high gage factor material is needed. Metal strain gages lack the sensitivity to detect very small signals without extremely clean electronics. Instead, we propose to use a semiconductor, either single-crystal or poly- silicon, to take advantage of their large gage factors. The drawback to semiconductor sensors is a higher resistivity, increasing thermal noise. To obtain an adequate sensor for our devices, we need to balance the resistivity and gage factor of deposited films, in the context of a procedure that is compatible with a stainless steel substrate. We discuss methods of installing highly sensitive semiconductor films on steel substrates in the following sections.

Table 3: System Model Parameters

Material	Constanten	SCS	p-poly	n-poly	$\alpha - Si : H$
Gage Factor	2.1	150	30	10	20
S_{bridge} (V/ϵ)	12.6	900	180	60	120
Film Thickness (μm)	0.5	2.0	2.0	1.0	1.0
Resistivity (Ω-cm)	4.9×10^{-5}	0.05	1.0	0.006	1.0
Gage resistance ($k\Omega$)	0.49	2.5	25	0.3	25
Total noise (μV)	1.1	1.4	3.1	1.1	3.1
Resolution ($n\epsilon$)	91	1.6	17	19	26

4.2 Fabrication procedures

Using stainless steel as the substrate for MEMS-type semiconductor devices presents special constraints on a fabrication process. In a disk drive, the stiffness of the steel suspension is critical to producing a predictable and stable flying height for the read-write head. The sensor must not add significant stiffness to the suspension, and its fabrication process should not alter the properties of the stainless steel. This calls for a fabrication process that takes place at temperatures below typical steel phase transition temperatures. We choose to avoid processing steps that take place above 600° C. In addition, if the sensor is to be built in the high strain hinge region, it must be able to withstand being strained as much as 10% during the metal forming process. The fabrication procedure must either withstand this treatment or produce a structure with sufficient sensitivity to be located at a sub-optimal location.

We examine two methods of forming piezoresistive strain gages on steel. The first is to deposit piezoresistive material on the steel substrate directly, via a low-temperature polysilicon or amorphous silicon deposition process. The second is to build sensors on a silicon handle substrate and transfer the sensors to the steel substrate via a bonding process. The first method is much simpler, but the materials available are limited, while the second method is more complicated and possibly more expensive, but permits the use of a wider range of materials, particularly single crystal silicon.

Fig. 8 shows the process flow for a piezoresistive film deposited directly on the steel substrate. In this case, the steel substrate is immediately coated with an insulating layer and the piezoresistive film (a). Potential insulating layers include spin-on-glass, PECVD silicon oxide, anodized aluminum, and spin-on polymers. Potential piezoresistive films include PECVD poly- or amorphous silicon and sputtered silicon films. The sensors are patterned by a wet silicon etchant (b) and an aluminum film is evaporated onto the wafer to form leads and bond pads (c). After interconnect patterning (d), the sensors and leads are protected by photoresist during patterning of the hinge from the wafer, also performed by wet etching.

Fig. 9 shows the proposed process flow for bonded sensors, using metal-to-metal bonding techniques of Microassembly

Technologies, Inc. A wafer with handle, sacrificial, and piezoresistive layers is used to form the sensors (a). The piezoresistive film is patterned into sensors connect to larger anchor pads by thin tethers (b). The sensors are undercut by etching the sacrificial layer, leaving them connected just by the tethers to the fixed tethers (c). A special metal alloy bonding material is deposited (d) and patterned into bumps at the bond locations (e). Meanwhile, an insulting film and a thin landing layer of gold or platinum are deposited onto the steel substrate and patterned as interconnects and external bond pads. The two substrates are then aligned and pressed together at 300° C, forming a low temperature weld where bumps meet the landing layer (f). Finally, the handle wafer is removed, breaking the tethers and leaving the sensors attached to the steel substrate (g).

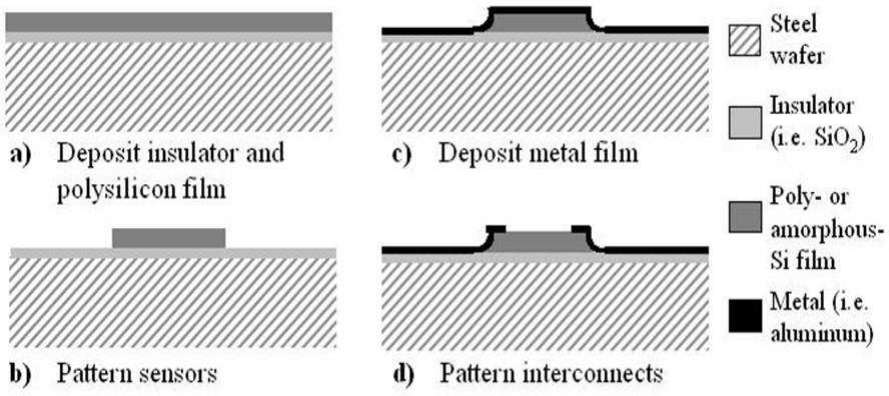

Figure 8: Fabrication procedure for directly deposited piezoresistive film

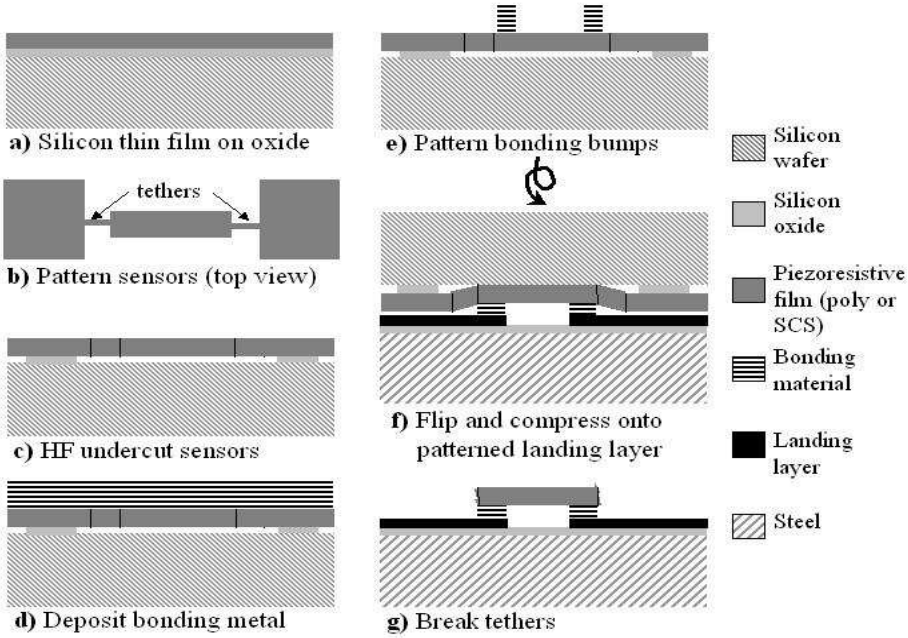

Figure 9: Fabrication procedure for bonded piezoresistive film

4.3 Experimental results

Our first tests of direct piezoresistor deposition involved highly-doped, sputtered silicon, followed by performed several experiments to improve the quality of the resulting film. Sputtered silicon was selected for it's extreme simplicity of deposition and compatibility with steel substrates. In our initial feasibility test, we deposited silicon from a lightly doped silicon target onto a substrate coated with PECVD silicon oxide. We patterned the sensors with Bell Labs silicon etchant (33% H_2O:3% NH_4F:64% HNO_3) and used aluminum interconnects, etched with Type A Aluminum Etchant. Fig. 10 shows one completed strain gage. The steel wafer was then cut into cantilever beams, and changes in resistance for fixed deflections measured at a probe station. We measured an excellent gage factor for the completed sensors of 25, but a resistivity of approximately 5000 Ohm-cm, producing an unacceptable level of thermal noise for high resolution sensing.

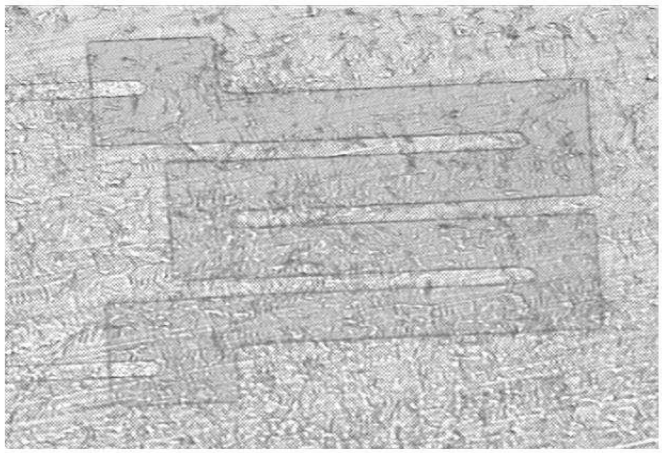

Figure 10: Strain gage fabricated from sputtered silicon

Subsequent tests with sputtered silicon focused on reducing resisitivity of the sputtered film. A Boron-doped target with bulk resistivity of 0.0002 Ω was installed for these tests. Base pressure, sputtering pressure, and sputtering power were varied for 20 minute sputtering periods. The lowest resistivity obtained on a consistent basis was 120 Ω, obtained at sputtering pressure of 10 mTorr at a low sputtering power, 100 W. We also observed that for the more conductive film, gage factor dropped to 15. Projected sensor resolution for a 2 μm thick film under these conditions is approximately 200 nanostrain, still several times higher than desired.

Conductivity of a sputtered semiconductor film is limited by the unordered nature of the film, low dopant activation, and inclusion of sputtering gas in the film. We also observed that base pressure of the sputtering machine prior to deposition was of critical importance to film quality (Fig. 11). This implies that contamination during the sputtering process is a major limitation to the process. We attempted to improve the film quality. conditions through both rapid thermal annealing (RTA) and long low temperature furnace anneals. For RTA, we annealed samples of the sputtered film in forming gas for time periods ranging from 30 seconds to 6 minutes, at temperatures from 400 C to 1000 C. At best, conductivity of the sputtered film increased by 5

% after a 1 minute anneal at 600°C, while above 800 C, the film abruptly stopped conducting, also suggesting problems with contamination. A

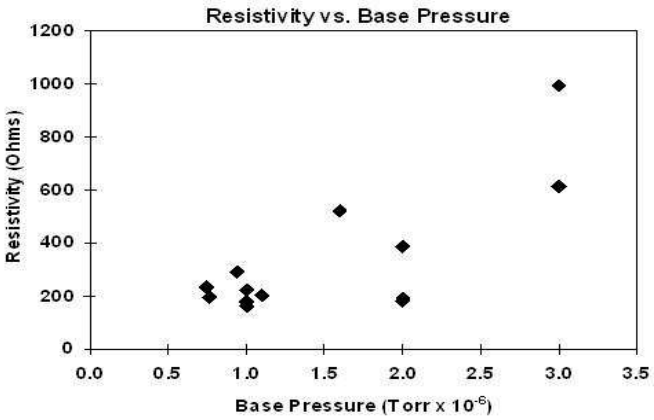

Figure 11: Strain gage fabricated from sputtered silicon

More conductive low-temperature polycrystalline and amorphous silicon films have been demonstrated for transistor applications via techniques such as very-high frequency plasma-enhanced chemical vapor deposition [], catalytic chemical vapor deposition [17], and laser crystallized polysilicon [18]. Hydrogenated amorphous silicon (α-Si:H) deposited by glow discharge, in particular, has been evaluated for its piezoresistive properties [19]. These techniques are more expensive than simple sputtering, but they may be explored as alternative direct deposition methods.

Protoype sensors fabricated by the bonding method are currently under construction. For this procedure, a standard LPCVD polysilicon film deposited on a silicon oxide sacrificial layer or a silicon-on-insulator (SOI) wafer with single crystal device layer may be used. In these cases, the gage factors and resistivities of the films are well-defined, and the Microassembly, Inc. bonding procedure is well-established for standard semiconductor substrates. The primary item of interest is the suitability of the bonding procedure for a steel substrate with a potentially non-standard insulating layer. The current batch of test structures includes steel wafers coated with spin-on-glass, anodized aluminum, and oxidized titanium insulating films, all of which may be deposited or formed at temperatures below 600 C.

5 Piezoelectric Sensors

An alternative to piezoresistive strain sensing is the use of piezoelectric films, which produce a voltage change when strained. In this section, we explore the use of piezoelectric materials as a strain gages in an instrumented suspension.

5.1 Theory

When a piezoelectric element is strained, the internal dielectric polarization is altered, producing an electric displacement and electric field across the element. For a thin film strained in the in-plane direction, the electric displacement is approximately

$$D_3 = d_{31} E_{11} \epsilon_1 \tag{42}$$

D_3 is the electric displacement in the out-of-plane direction in Coulombs/m^2, d_{31} is the piezoelectric constant from the in-plane to out-of-plane direction, E_{11} is the elastic modulus of the film in the in-plane direction, and ϵ_1 is the in-plane strain. The resulting change in voltage depends on the capacitance of the sensor, giving voltage change

$$V = \frac{d_{31} E_{11} t}{\varepsilon_{33}} \tag{43}$$

where t is the thickness of the sensor and ε_{33} is the dielectric constant of the film in the out-of-plane direction. The sensitivity of the sensor is then

$$S = \frac{V}{\epsilon_1} = \frac{d_{31} E_{11} t}{\varepsilon_{33}} \tag{44}$$

It is clear from this equation that reducing a piezoelectric material to a thin film greatly reduces its potential sensitivity. However, the intrinsic noise in the sensor is that of an equivalent capacitor, and hence negligible when low frequencies are filtered out. As a result, the piezoelectric sensor does not suffer from the intrinsic noise limitations of the piezoresistive sensors discussed in the previous section.

Table 4 lists estimated sensitivities and resolutions for piezoelectric thin films, assuming electronics noise of 9 nV/$\sqrt{Hz}$ over a 20 kHz bandwidth, and negligible instrinsic noise. The sensors are assumed to be 2 μm thick and 100 μm square. Under these conditions, most strong piezoelectrics appear capable of nanometer-level strain resolution. Lead-zirconium-titanate (PZT) is a very common material, but thin film deposition is complex. Instead, we have begun experimentation with zinc oxide, which also meets our performance specifications, but is more easily deposited in a piezoelectric form. Polymer PVDF is also easily applied, but requires a large polarizing electric field.

5.2 Fabrication procedure

The fabrication procedure for zinc oxide sensors on a steel substrate is shown in figure **??**. Spin-on-glass is first applied to planarize the wafer surface. A chrome adhesion layer and gold seed layer prepare the substrate for zinc oxide deposition and act as the lower electrode of the sensor (a). Zinc oxide is then sputtered in 50:50 $Ar : O_2$ plasma at 200 C. The zinc oxide is capped with a metal film that acts as an etch stop during wet etching (b). Sensors are patterned and etched in by a wet etchant. A second layer of spin on glass is applied to separate the upper and lower electrodes and contact holes are patterned and etched

Table 4: System Model Parameters

Material	PZT	Zinc Oxide	PVDF
d_{31} $(C/N \times 10^{-12})$	-123	5.2	23
Young's modulus (GPa)	53	210	3
Relative permitivity	1700	12	12
Sensitivity (V/ϵ)	1200	24500	1300
Noise (μV)	1.3	1.3	1.3
Resolution (nϵ)	1.1	0.5	1.0

in dilute hydroflouric acid (d-e). Finally, an aluminum layer is evaporated and patterned aluminum etchant to form the upper electrode (f).

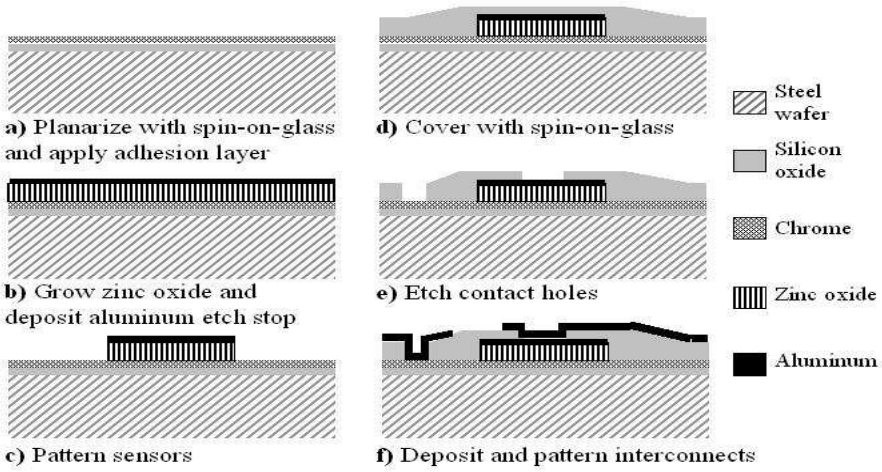

Figure 12: Fabrication procedure for zinc oxide piezoelectric strain gage

5.3 Experimental results

Zinc oxide films have been deposited on both single-crystal silicon and stainless steel wafers by the sputtering process described above. The piezoelectric response of the films was tested using a tapper that measures the current generated by an oscillating probe indenting the ZnO film from above an electrode. Tapper measurements indicated a piezoelectric coefficient on the single crystal silicon substrate of $5 \times 10^{-12} C/N$.

The roughness of a stainless steel wafer, with mean value of approximately 20 nm rms, prevents the formation of a high

quality zinc oxide film directly on steel. However, we find that spin-on-glass provides adequate planarization of the wafer surface to obtain a piezoelectric response. Excellent results were obtained in unpatterned specimens for spin-on-glass that was densified at 350 C in the sputtering chamber prior to zinc oxide deposition. From tapper measurements, we estimate the d_{31} coefficient for these samples to be 1 C/N. The reduction in performance is likely a result of imperfections of the zinc oxide film from any remaining surface imperfections after spin-on-glass application, but even this level of piezoelectric response projects to resolution better than 1 nanostrain. Fig. 13 shows a cross-section of the deposited zinc oxide over spin-on glass. The planarization from the lowest layer, steel, to middle glass layer is visible, as is the columnar structure of the top zinc oxide layer.

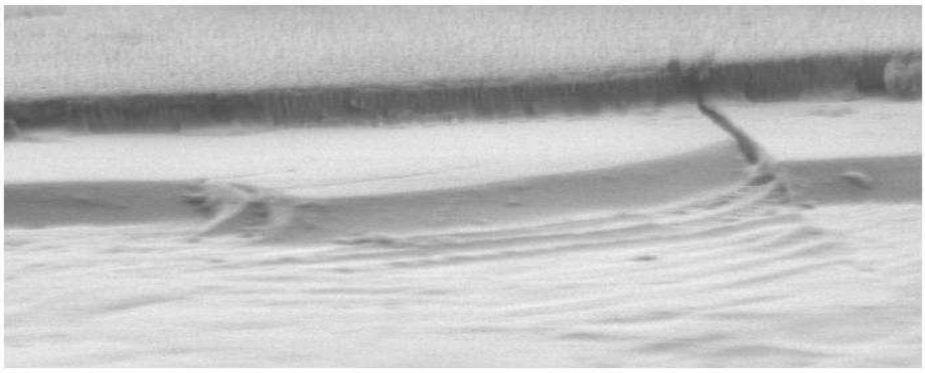

Figure 13: Zinc oxide film on steel wafer planarized with spin-on glass

We are currently testing patterned sensors to confirm sensitivity of the film after performing the remaining processing steps of the fabrication procedure.

6 Conclusions and Future Work

In this paper we have examined the design and fabrication of an instrumented disk drive suspension. We proposed the optimization of sensor location based on the cost function of an LQG controller and filter. An approximation for the cost function is derived for low-cost control in a noisy system to reduce computational complexity and gain insight into optimization results. The optimal location for a single strain gage on the Hutchinson 3430 suspension was identified on the upper inside of the hinge region, with good agreement between exact and approximate optimization methods.

Both piezoresistive and piezoelectric films were discussed as sensor materials, with testing of both types of sensor ongoing. Sputtered silicon films on steel were found to have adequate gage factor but intrinsic noise limitations due to low conductivity.

Bonded silicon films will provide more precise control of film properties and even higher sensitivities. Prototype bonded strain gages are currently under construction. Piezoelectric zinc oxide films have also been deposited on steel wafers with excellent sensitivity, and are currently being evaluated after complete sensor patterning.

Future improvements to the instrumented suspension design involves refinement of both sensor optimization and fabrication. The simplifying approximations introduced for the optimization scheme may be used to quickly evaluate multiple sensor schemes. To accomodate more robust controller designs, it will also be useful to adapt the optimization scheme to reject strain sources, such as suspension bending modes, that do not correspond to off-track motion at the read/write head. Meanwhile, additional piezoresistive materials may be evaluated for directly deposited sensors, and new combinations of underlying insulators and bonding conditions may be examined to improve reliability of bonded sensors. With regards to piezoelectric sensors, response and measurement in an electronically-noisy environment must be evaluated. Finalized sensor locations and fabrication techniques will be used to assemble a full instrumented suspension for integration in a dual-stage disk drive servo system.

References

[1] Huang, Y., M. Banther, P. Mathur and W. Messner, Design and analysis of a high bandwidth disk drive servo system using and instrumented suspension, *IEEE/ASME Transactions on Mechatronics*, vol. 4, no. 2, 1999, pp. 196-206.

[2] Huang, F.Y., T. Semba, W. Imaino and F. Lee, Active damping in hdd actuator, *IEEE Transactions on Magnetics*, vol. 37, no. 2, 2001, pp. 847-849.

[3] Y. Li and R. Horowitz and R. Evans, Vibration control of PZT actuated suspension dual-stage servo system using a PZT sensor, *IEEE Transactions on Magnetics*, vol. 30, no. 2, 2003, pp. 932-936.

[4] A. Hac and L. Liu, Sensor and actuator location in motion control of flexible structures, *Journal of Sound and Vibration*, vol. 167, no. 2, 1993, pp 239-261.

[5] M. Banther and Y. Huang and W. Messner, "Optimal strain gage placement for an instrumented disk drive suspension", *Proc. American Control Conference*, Philadelphia, PA, 1998, pp. 3023-3027.

[6] Gross, H., University of California, Berkeley, dissertation, Berkeley, CA, 1988.

[7] J.N. Juang and G. Rodriguez, "Formulations and applications of large structure actuator and sensor placements", *Proc. YPI&SU/AIAA Symposium on Dynamics and Control of Large Flexible Spacecraft*, 1979, pp. 247-262.

[8] Hiramoto, K., H. Doki, and G. Obinata, Optimal sensor/actuator placement for vibration control using explicit solution of algebraic Riccati equation. *Journal of Sound and Vibrataion* Vol. 229, No. 5, 2000, pp.1057-1075.

[9] Kondoh, S., C. Yatomi, and K.Inoue, The positioning of sensors and actuators in the vibration of flexible systems, *JSME International Journal*, vol. 33, 1990, pp. 145-152.

[10] Yamaguchi, Y., K. Takahashi, and H. Fujita, Flow induced vibration of magnetic head suspension in hard disk drive. *IEEE Transactions on Magnetics*, Vol. 22, No. 5, 1986, pp.1022-1024.

[11] Shimizu, H., T. Shimizu, M. Tokuyama, H. Masuda, and S. Nakamura, Numerical simulation of positioning error caused by air-flow-induced vibration of head gimbals assembly in hard disk drive. *IEEE Transaactions on Magnetics*, Vol. 39, No. 2, 2003, pp.806-811.

[12] Shaked, U., Explicit solution to the singular discrete-time stationary linear filtering problem. *IEEE Transactions on Automatic Control*, Vol. AC-30, No.1, 1985, pp. 34-47.

[13] Yen, J.Y., University of California, Berkeley, dissertation: Identification and control of a computer disk drive actuator, Berkeley, CA, 1988.

[14] Athans, M. A tutorial on the LQG/LTR design method. *Proc. of 1986 American Controls Conference*, vol. 2, 1986, pp.1289-1296.

[15] Mason, W.P., *Crystal Properties of Interaction Processes*, Academic Press, New York; 1966.

[16] Obermeier, E. and P. Kopyztynski, Polysilicon as a material for microsensor applications, *Sensors & Actuators A - Physical* Vol. 30 No.1 pp. 149-155.

[17] Sakai, M., T. Tsutsumi, T. Yoshioka, A. Masuda, and H. Matsamura, High performance amorphous-silicon thin film transistors prepared by catalytic chemical vapor deposition with high deposition rate. *Thin Solid Films*, vol. 395, 2001, pp.330-334.

[18] Fulks, R.T., J. Ho, and J.B. Boyce, "A new self-aligned top-gate polysilicon TFT architecture for low temperature processing". *55th Annual Device Research Conf.* Fort Collins, CO, 1997, pp.103-104.

[19] Spear, W.E. and M. Heintze, The effects of applied and internal strain on the electronic properties of amorphous silicon. *Philosophical Magazine B-Physics of Condensed Matter Structural Electronic Optical & Magnetic Properties*, vol.54, no.5, 1986, pp. 343-58.

[]

We derive analytical bounds for certain terms of the error coefficient matrix M of of the Kalman filter Riccati equation

$$AM + MA^T - MC(\Phi)^T \mathrm{v}^{-1} C(\Phi)M + B_w \mathrm{w} B_w^T = 0 \tag{45}$$

for a system in modal coordinates with force inputs and displacement outputs. Under certain conditions, the bounds on the will lead provide an approximation for the LQG objective function with cheap control, which simplifies to

$$J_{H2} \rightarrow tr\left[MD^T D\right] = \sum_i \sum_j m_{2i-1,2j-1} d_i d_j \tag{46}$$

The system to be examined has state space form

$$\begin{aligned} \dot{x} &= Ax + Bu + B_w w && (47)\\ y &= Cx + v && (48)\\ E[w^T w] &= \mathrm{w} I_{l\times l} && (49)\\ E[v^T v] &= \mathrm{v} I_{r\times r} && (50)\\ & && (51) \end{aligned}$$

with

$$A = \begin{bmatrix} A_1 & 0 & \cdots & 0 \\ 0 & A_2 & & \vdots \\ \vdots & & \ddots & \\ & & & A_n \end{bmatrix} \tag{52}$$

$$A_i = \begin{bmatrix} 0 & \omega_i \\ -\omega_i & -2\xi_i\omega_i \end{bmatrix} \tag{53}$$

$$B_w = \begin{bmatrix} 0 & \cdots & 0 \\ b_{11}\omega_1 & \cdots & b_{1l}\omega_1 \\ 0 & \cdots & 0 \\ b_{21}\omega_2 & \cdots & b_{2l}\omega_2 \\ \vdots & & \vdots \\ 0 & \cdots & 0 \\ b_{n1}\omega_n & \cdots & b_{nl}\omega_n \end{bmatrix} \tag{54}$$

$$C(\Phi) = \begin{bmatrix} c_{11}(\Phi_1) & 0 & c_{12}(\Phi_1) & 0 & \cdots & c_{1n}(\Phi_1) & 0 \\ \vdots & \vdots & \vdots & \vdots & & \vdots & \vdots \\ c_{r1}(\Phi_r) & 0 & c_{r2}(\Phi_r) & 0 & \cdots & c_{rn}(\Phi_r) & 0 \end{bmatrix} \tag{55}$$

We will first perform the approximation for a undamped SISO system with $n = 2$ to demonstrate procedure. Then we will consider undamped and damped MIMO cases and finally apply the results in discrete time.

.0.1 2 modes, undamped

Consider a system of 2 undamped modes with a single disturbance and sensor. The Riccati equation in (45) results in the following set of 10 equations for the 10 independent components of matrix M:

Diagonal block 1,1:

$$(1,1) \quad : \quad 2\omega_1 m_{12} - (c_1 m_{11} + c_2 m_{13})^2 \frac{1}{\mathrm{v}} = 0 \tag{56}$$

$$(1,2) \quad : \quad \omega_1(m_{22} - m_{11}) - (c_1 m_{11} + c_2 m_{13})(c_1 m_{12} + c_2 m_{23})\frac{1}{\mathrm{v}} = 0 \tag{57}$$

$$(2,2) \quad : \quad -2\omega_1 m_{12} - (c_1 m_{12} + c_2 m_{23})^2 \frac{1}{\mathrm{v}} + b_1^2 \omega_1^2 \mathrm{w} = 0 \tag{58}$$

Diagonal block 2,2:

$$(3,3) \quad : \quad 2\omega_2 m_{34} - (c_1 m_{13} + c_2 m_{33})^2 \frac{1}{\mathrm{v}} = 0 \tag{59}$$

$$(3,4) \quad : \quad \omega_2(m_{44} - m_{33}) - (c_1 m_{13} + c_2 m_{33})(c_1 m_{14} + c_2 m_{34})\frac{1}{\mathrm{v}} = 0 \tag{60}$$

$$(4,4) \quad : \quad -2\omega_2 m_{34} - (c_1 m_{14} + c_2 m_{34})^2 \frac{1}{\mathrm{v}} + b_2^2 \omega_2^2 \mathrm{w} = 0 \tag{61}$$

Cross-term block 1,2:

$$(1,3) \quad : \quad \omega_1 m_{23} + \omega_2 m_{14} - (c_1 m_{11} + c_2 m_{13})(c_1 m_{13} + c_2 m_{33})\frac{1}{\mathrm{v}} = 0 \tag{62}$$

$$(1,4) \quad : \quad \omega_1 m_{24} - \omega_2 m_{13} - (c_1 m_{11} + c_2 m_{13})(c_1 m_{14} + c_2 m_{34})\frac{1}{\mathrm{v}} = 0 \tag{63}$$

$$(2,3) \quad : \quad -\omega_1 m_{13} + \omega_2 m_{24} - (c_1 m_{12} + c_2 m_{23})(c_1 m_{13} + c_2 m_{33})\frac{1}{\mathrm{v}} = 0 \tag{64}$$

$$(2,4) \quad : \quad -\omega_1 m_{14} - \omega_2 m_{23} - (c_1 m_{12} + c_2 m_{23})(c_1 m_{14} + c_2 m_{34})\frac{1}{\mathrm{v}} + b_1 b_2 \omega_1 \omega_2 \mathrm{w} = 0 \tag{65}$$

From (56) and (59), we know

$$m_{12} \quad \geq \quad 0 \tag{66}$$

$$m_{34} \quad \geq \quad 0 \tag{67}$$

Since

$$(c_1 m_{12} + c_2 m_{23})^2 \quad \geq \quad 0 \tag{68}$$

$$(c_1 m_{11} + c_2 m_{13})^2 \quad \geq \quad 0 \tag{69}$$

each of the first two terms in (58) must be less than or equal to $b_1^2\omega_1^2 w$, giving

$$m_{12} \leq \frac{b_1^2\omega_1 \mathrm{w}}{2} \tag{70}$$

and combining (56) and (58):

$$|c_1 m_{11} + c_2 m_{13}| \leq |b_1|\omega_1\sqrt{\mathrm{wv}} \tag{71}$$

$$|c_1 m_{12} + c_2 m_{23}| \leq |b_1|\omega_1\sqrt{\mathrm{wv}} \tag{72}$$

Similarly, from the second diagonal block:

$$m_{34} \leq \frac{b_2^2\omega_2 \mathrm{w}}{2} \tag{73}$$

$$|c_1 m_{13} + c_2 m_{33}| \leq |b_2|\omega_2\sqrt{\mathrm{wv}} \tag{74}$$

$$|c_1 m_{14} + c_2 m_{34}| \leq |b_2|\omega_2\sqrt{\mathrm{wv}} \tag{75}$$

Now multiply (63) by $-\omega_2$ and (64) by ω_1 and add them together, to get

$$\begin{aligned} m_{13}(\omega_2^2 - \omega_1^1) &= -\omega_2(c_1 m_{11} + c_2 m_{13})(c_1 m_{14} + c_2 m_{34})\frac{1}{\mathrm{v}} \\ &\quad + \omega_1(c_1 m_{12} + c_2 m_{23})(c_1 m_{13} + c_2 m_{33}\frac{1}{\mathrm{v}} \end{aligned} \tag{76}$$

Using the largest possible bounds from (71),(72),(74), and (75) ,

$$|m_{13}| \leq \frac{|b_1 b_2|\omega_1\omega_2 \mathrm{w}(\omega_2 + \omega_1)}{\omega_2^2 - \omega_1^2} = \frac{|b_1 b_2|\omega_1\omega_2 \mathrm{w}}{\omega_2 - \omega_1} \tag{77}$$

Similarly,

$$|m_{24}| \leq \frac{|b_1 b_2|\omega_1\omega_2 \mathrm{w}(\omega_2 + \omega_1)}{\omega_2^2 - \omega_1^2} = \frac{|b_1 b_2|\omega_1\omega_2 \mathrm{w}}{\omega_2 - \omega_1} \tag{78}$$

Including the $b_1 b_2 \omega_1 \omega_2 \mathrm{w}$ term in (65) raises the bound on m_{14} and m_{23}:

$$|m_{14}| \leq \frac{|b_1 b_2|\omega_1\omega_2 \mathrm{w}(\omega_2 + 2\omega_1)}{\omega_2^2 - \omega_1^2} \tag{79}$$

$$|m_{23}| \leq \frac{|b_1 b_2|\omega_1\omega_2 \mathrm{w}(2\omega_2 + \omega_1)}{\omega_2^2 - \omega_1^2} \tag{80}$$

Now, return to (58) and solve for m_{12}

$$m_{12} = \frac{1}{2\omega_1}\left\{b_1^2\omega_1^2 \mathrm{w} - (c_1 m_{12} + c_2 m_{23})^2 \frac{1}{\mathrm{v}}\right\} \tag{81}$$

Using the bounds from (70) and (80) in (81),

$$m_{12} \geq \frac{1}{2\omega_1}\left\{b_1^2\omega_1^2\mathrm{w} - \left(|c_1|\max(m_{12}) + |c_2|\max(m_{23})\right)^2\frac{1}{\mathrm{v}}\right\} \tag{82}$$

$$= \frac{1}{2\omega_1}\left\{b_1^2\omega_1^2\mathrm{w} - \left(|c_1|\left[\frac{b_1^2\omega_1\mathrm{w}}{2}\right] + |c_2|\left[\frac{|b_1b_2|\omega_1\omega_2\mathrm{w}(2\omega_2+\omega_1)}{\omega_2^2-\omega_1^2}\right]\right)^2\frac{1}{\mathrm{v}}\right\} \tag{83}$$

Factoring out like terms

$$m_{12} \geq \frac{b_1^2\omega_1\mathrm{w}}{2}\left\{1 - \frac{\mathrm{w}}{\mathrm{v}}\left(\frac{|c_1b_1|}{2} + |c_2b_2|\frac{\omega_2(\omega_1+2\omega_2)}{\omega_2^2-\omega_1^2}\right)^2\right\} \tag{84}$$

In full, we have from (70) and (84)

$$\frac{b_1^2\omega_1\mathrm{w}}{2} \geq m_{12} \geq \frac{b_1^2\omega_1\mathrm{w}}{2}\left\{1 - \frac{\mathrm{w}}{\mathrm{v}}\left(\frac{|c_1b_1|}{2} + |c_2b_2|\frac{\omega_2(\omega_1+2\omega_2)}{\omega_2^2-\omega_1^2}\right)^2\right\} \tag{85}$$

If the terms inside the brackets in (85) are small, we have a narrow bound on the value of m_{12}. Furthermore, minimum value of m_{12} may be used to estimate m_{11} by comparing the size of the terms in (56). If

$$2\omega_1 m_{12} \gg \frac{(c_2m_{13})^2}{\mathrm{v}} \tag{86}$$

then

$$2\omega_1 m_{12} \approx \frac{(c_1m_{11})^2}{\mathrm{v}} \tag{87}$$

Equation (86) is satisfied if

$$2\omega_1\min(m_{12}) \gg \frac{(c_2\max(m_{13}))^2}{\mathrm{v}} \tag{88}$$

Writing out (88) with (84) gives

$$b_1^2\omega_1^2\mathrm{w}\left\{1 - \frac{\mathrm{w}}{\mathrm{v}}\left(\frac{|c_1b_1|}{2} + |c_2b_2|\frac{\omega_2(\omega_1+2\omega_2)}{\omega_2^2-\omega_1^2}\right)^2\right\} \gg \frac{c_2^2b_1^2b_2^2\omega_1^2\omega_2^2\mathrm{w}^2}{(\omega_2^2-\omega_1^2)^2\mathrm{v}} \tag{89}$$

and simplified,

$$1 - \left(\frac{1}{2}|c_1b_1|\sqrt{\frac{\mathrm{w}}{\mathrm{v}}} + \frac{\omega_2(\omega_1+2\omega_2)}{\omega_2^2-\omega_1^2}|c_2b_2|\sqrt{\frac{\mathrm{w}}{\mathrm{v}}}\right) \gg \frac{\omega_2^2}{\omega_2^2-\omega_1^2}|c_2b_2|\sqrt{\frac{\mathrm{w}}{\mathrm{v}}} \tag{90}$$

For a system with well-spaced natural frequencies, (90) is true if

$$|c_1b_1|\sqrt{\frac{\mathrm{w}}{\mathrm{v}}} \ll 1 \tag{91}$$

$$|c_2b_2|\frac{\mathrm{w}}{\mathrm{v}} \ll 1 \tag{92}$$

Under these conditions, we also see that m_{12} can be approximated by its upper bound in (85) and then used to solve for m_{11} from (87):

$$m_{11} \approx |\frac{b_1}{c_1}|\omega_1\sqrt{\mathrm{wv}} \tag{93}$$

Finally, compare the approximate value of m_{11} to the maximum value of m_{33}. Adding the condition

$$|c_1 b_2|\sqrt{\frac{\mathrm{w}}{\mathrm{v}}} \ll 1 \tag{94}$$

implies that for widely spaced natural frequencies

$$m_{11} \approx \frac{|b_1|}{|c_1|}\omega_1\sqrt{\mathrm{wv}} \gg \frac{|b_1 b_2|\omega_1\omega_2\mathrm{w}}{\omega_2 - \omega_1} \geq m_{13} \tag{95}$$

To summarize, under the conditions of widely spaced natural frequencies and proper sizes of w,v,c_1,c_2,b_1, and b_2, we have an approximation for m_{11} and confidence that $m_{11} \gg m_{13}$. A similar derivation, with a fourth condition

$$|c_2 b_1|\sqrt{\frac{\mathrm{w}}{\mathrm{v}}} \ll 1 \tag{96}$$

would give

$$m_{22} \approx |\frac{b_2}{c_2}|\omega_2\sqrt{\mathrm{wv}} \gg m_{13} \tag{97}$$

This provides information about all of the coefficients of M that appear in the LQG cost function for cheap control, and thus we could evaluate the approximate value of the cost function without solving any Riccati equations. The following section generalizes these results for a MIMO system.

.0.2 MIMO, undamped

Now consider the undamped MIMO case with n modes, l disturbances, r sensors, and $\xi_i = 0\ \forall i$. We will again examine the Riccati equation in (45) to form bounds similar to those from the 2x2 SISO case.

First, the nonzero $B_w W B_w$ terms in the MIMO Riccati equation can be bounded as

$$(b_{i1}b_{j1} + \cdots + b_{il}b_{jl})\omega_i\omega_j w \leq (|b_{i1}| + \cdots + |b_{i1}|)(|b_{j1}| + \cdots + |b_{jl}|)\omega_i\omega_j w \tag{98}$$

$$\omega_i\omega_j\mathrm{w}\sum_{k=1}^{l} b_{ik}b_{jk} \leq \omega_i\omega_j\mathrm{w}\sum_{k=1}^{l}|b_{ik}|\sum_{p=1}^{l}|b_{jp}| \tag{99}$$

This is a loose bound but has little effect on the final conclusion and simplifies notation using variables b'

$$b'_i = \sum_{k=1}^{l}|b_{ik}| \tag{100}$$

The 2 by 2 on-diagonal block of the Riccati equation corresponding to mode i gives the equations:

$$(2i-1,2i-1) \quad : \quad 2\omega_i m_{2i-1,2i-1} - \frac{1}{\mathrm{v}}\sum_{k=1}^{r}\left(\sum_{p=1}^{n} c_{kp} m_{2i-1,2p-1}\right)^2 = 0 \tag{101}$$

$$(2i-1,2i) \quad : \quad \omega_i(m_{2i,2i} - m_{2i-1,2i-1}) - \frac{1}{\mathrm{v}}\sum_{k=1}^{r}\left[\left(\sum_{p=1}^{n} c_{kp} m_{2i-1,2p-1}\right)\left(\sum_{q=1}^{n} c_{kq} m_{2i,2q-1}\right)\right] = 0 \tag{102}$$

$$(2i,2i) \quad : \quad -2\omega_i m_{2i-1,2i} - \frac{1}{\mathrm{v}}\sum_{k=1}^{r}\left(\sum_{p=1}^{n} c_{kp} m_{2i,2p-1}\right)^2 + \omega_i^2 \mathrm{w}\sum_{k=1}^{l} b_{i1}^2 = 0 \tag{103}$$

As for the SISO case, the squared terms from $MC^T\mathrm{v}^{-1}CM$ imply that $m_{2i-1,1} > 0$ for all i, and therefore none of the terms in (103) can exceed $\omega_i^2 \mathrm{w}\sum_{k=1}^{l} b_{ik}^2$. Hence,

$$m_{2i-1,2i} \leq \frac{\omega_i \mathrm{w}}{2}\sum_{k=1}^{l} b_{i1}^2 \leq (b_i')^2\frac{\omega_i \mathrm{w}}{2} \tag{104}$$

Each of the $C^T M$ terms may also be bounded

$$\left|\sum_{p=1}^{n} c_{kp} m_{2i-1,2p-1}\right| \quad \leq \quad (b_i')\omega_i\sqrt{\mathrm{wv}} \tag{105}$$

$$\left|\sum_{p=1}^{n} c_{kp} m_{2i,2p-1}\right| \quad \leq \quad (b_i')\omega_i\sqrt{\mathrm{wv}} \tag{106}$$

The off-diagonal blocks of the Riccati equation between two modes, i and j, give the block of four equations

$$(2i-1,2j-1) \quad : \quad \omega_i m_{2i,2j-1} + \omega_j m_{2i-1,2j} - \frac{1}{\mathrm{v}}\sum_{k=1}^{r}\left[\left(\sum_{p=1}^{n} c_{kp} m_{2i-1,2p-1}\right)\left(\sum_{q=1}^{n} c_{kq} m_{2j-1,2q-1}\right)\right] = 0 \tag{107}$$

$$(2i-1,2j) \quad : \quad \omega_i m_{2i,2j} - \omega_j m_{2i-1,2j-1} - \frac{1}{\mathrm{v}}\sum_{k=1}^{r}\left[\left(\sum_{p=1}^{n} c_{kp} m_{2i-1,2p-1}\right)\left(\sum_{q=1}^{n} c_{kq} m_{2j,2q-1}\right)\right] = 0 \tag{108}$$

$$(2i,2j-1) \quad : \quad -\omega_i m_{2i-1,2j-1} + \omega_j m_{2i,2j} - \frac{1}{\mathrm{v}}\sum_{k=1}^{r}\left[\left(\sum_{p=1}^{n} c_{kp} m_{2i,2p-1}\right)\left(\sum_{q=1}^{n} c_{kq} m_{2j-1,2q-1}\right)\right] = 0 \tag{109}$$

$$\begin{aligned}(2i,2j) \quad : \quad & -\omega_i m_{2i-1,2j} - \omega_j m_{2i,2j-1} - \frac{1}{\mathrm{v}}\sum_{k=1}^{r}\left[\left(\sum_{p=1}^{n} c_{kp} m_{2i,2p-1}\right)\left(\sum_{q=1}^{n} c_{kq} m_{2j,2q-1}\right)\right] \\ & +\omega_i\omega_j \mathrm{w}\left(\sum_{k=1}^{l} b_{ik} b_{jk}\right) = 0\end{aligned} \tag{110}$$

Manipulating these equations to produce single ωm first terms, then bounding them with the largest possible combinations of bounds from (104) and (105) gives

$$|m_{2i-1,2j-1}| \quad \leq \quad |b_i' b_j'|\omega_i\omega_j \mathrm{w}\frac{r\omega_i + r\omega_j}{|\omega_j^2 - \omega_i^2|} \tag{111}$$

$$|m_{2i,2j}| \quad \leq \quad |b_i' b_j'|\omega_i\omega_j w\frac{r\omega_i + r\omega_j}{|\omega_j^2 - \omega_i^2|} \tag{112}$$

$$|m_{2i-1,2j}| \leq |b'_i b'_j|\omega_i\omega_j \mathrm{w}\frac{(r+1)\omega_i + r\omega_j}{|\omega_j^2 - \omega_i^2|} \tag{113}$$

$$|m_{2i,2j-1}| \leq |b'_i b'_j|\omega_i\omega_j \mathrm{w}\frac{r\omega_i + (r+1)\omega_j}{|\omega_j^2 - \omega_i^2|} \tag{114}$$

Solving for $m_{2i-1,2i}$ from (103) gives

$$m_{2i-1,2i} = \frac{1}{2\omega_i}\left\{\omega_i^2 \mathrm{w}\left(\sum_{k=1}^{l} b_{ik}^2\right) - \frac{1}{\mathrm{v}}\sum_{k=1}^{r}\left(\sum_{p=1}^{n} c_{kp} m_{2i,2p-1}\right)^2\right\} \tag{115}$$

$$\geq \frac{1}{2\omega_i}\left\{\omega_i^2 \mathrm{w}\left(\sum_{k=1}^{l} b_{ik}^2\right) - \frac{1}{\mathrm{v}}\sum_{k=1}^{r}\left(\sum_{p=1}^{n} |c_{kp}| \max(m_{2i,2p-1})\right)^2\right\} \tag{116}$$

$$= \frac{1}{2\omega_i}\left\{\omega_i^2 \mathrm{w}\left(\sum_{k=1}^{l} b_{ik}^2\right) - \frac{1}{\mathrm{v}}\sum_{k=1}^{r}\left(\sum_{p=1,p\neq i}^{n} |c_{kp}||b'_i b'_p|\omega_i\omega_p \mathrm{w}\frac{r\omega_i - (r+1)\omega_p}{|\omega_p^2 - \omega_i^2|} + |c_{ki}|(b'_i)^2\frac{\omega_i \mathrm{w}}{2}\right)^2\right\} \tag{117}$$

$$= \frac{\omega_i \mathrm{w}}{2}\left(\sum_{k=1}^{l} b_{il}^2\right)\left\{1 - \frac{\mathrm{w}}{\mathrm{v}}\sum_{k=1}^{r}\left(\sum_{p=1,p\neq i}^{n} |c_{kp}b'_p|\frac{|b'_i|}{\sqrt{\sum_{q=1}^{l} b_{iq}^2}}\omega_p\frac{r\omega_i - (r+1)\omega_p}{|\omega_p^2 - \omega_i^2|} + \right.\right.$$

$$\left.\left. + \frac{1}{2}|c_{ki}b'_i|\frac{|b'_i|}{\sqrt{\sum_{q=1}^{l} b_{iq}^2}}\right)^2\right. \tag{119}$$

For balanced inputs and widely spaced modes, the magnitudes of $\frac{|b'_i|}{\sqrt{\sum_{q=1}^{l} b_{iq}^2}}$ and $\omega_p\frac{r\omega_i-(r+1)\omega_p}{|\omega_p^2-\omega_i^2|}$ are typically low order. Then the size of the terms in this equation are driven by the magnitude of $|c_{kp}b'_p|^2\frac{\mathrm{w}}{\mathrm{v}}$ for any combination of k and p. These terms are small when the magnitude of sensor noise, v, is large compared to the combined mode excitation, $(b_{p1}^2 + \cdots + b_{pl}^2)\mathrm{w}$ multiplied by the sensor gains, $|c_{kp}|$. In this case, where

$$|c_{kq}b'_p|^2\frac{\mathrm{w}}{\mathrm{v}} \ll 1 \tag{120}$$

for all k and p,

$$m_{2i-1,2i} \to \frac{\omega_i \mathrm{w}}{2}\left(\sum_{k=1}^{l} b_{il}^2\right) \tag{121}$$

Now consider (101) and the importance of $m_{2i-1,2i-1}$ relative to the other terms of M. If for all k and all $j \neq i$,

$$\frac{1}{\mathrm{v}}(|c_{kj}|m_{2i-1,2j-1})^2 \ll 2\omega_i m_{2i-1,2i} \tag{122}$$

then MC^T terms are dominated by the diagonal elements of M. Using the approximation in (121), this condition may be stated as

$$\frac{1}{\mathrm{v}}\left(|c_{kj}|\max(m_{2i-1,2j-1})\right)^2 \ll (b_{i1}^2+\cdots+b_{il}^2)\omega_i^2\mathrm{w} \tag{123}$$

or

$$\frac{1}{\mathrm{v}}\left(|c_{kj}||b_i'b_j'|\omega_i\omega_j w\frac{r\omega_i+r\omega_j}{|\omega_j^2-\omega_i^2|}\right) \ll (b_{i1}^2+\cdots+b_{il}^2)^2\omega_i^2\mathrm{w} \tag{124}$$

$$|c_{kj}b_j'|^2\frac{w}{v}\left(\frac{b_i'}{\sqrt{\sum_{k=1}^l b_{il}^2}}\right)\left(\frac{r\omega_j}{\omega_j-\omega_i}\right)^2 \ll 1 \tag{125}$$

This condition is fulfilled by the same conditions imposed to get the approximation of $m_{2i-1,2i}$: widely-spaced modes, balanced inputs, and (120) satisfied. Therefore, $m_{2i-1,2i-1}$ does indeed dominate (**??**) under such conditions. Assuming all other terms from M are negligible and solving the (101) for $m_{2i-1,2i-1}$ with $m_{2i-1,2i}$ from (121), we obtain

$$m_{2i-1,2i-1} \approx \frac{\sqrt{\sum_{p=1}^l b_{ip}^2}\omega_i\sqrt{\mathrm{wv}}}{\sqrt{\sum_{k=1}^r c_{1i}^2}} \tag{126}$$

The objective function for low cost control is now

$$J_{H2} = \sum_{i=1}^n \frac{d_{ii}^2\sqrt{\sum_{p=1}^l b_{ip}^2}\omega_i\sqrt{\mathrm{wv}}}{\sqrt{\sum_{k=1}^r c_{1i}^2}} \tag{127}$$

.0.3 Damping

When damping is included in the system, the blocks of equations from the Riccati equation become:

$$(2i-1,2i-1) \;:\; 2\omega_i m_{2i-1,2i-1} - \frac{1}{\mathrm{v}}\sum_{k=1}^r\left(\sum_{p=1}^n c_{kp}m_{2i-1,2p-1}\right)^2 = 0 \tag{128}$$

$$(2i-1,2i) \;:\; -2\xi_i\omega_i m_{2i-1,2i} + \omega_i(m_{2i,2i}-m_{2i-1,2i-1}) - \frac{1}{\mathrm{v}}\sum_{k=1}^r\left[\left(\sum_{p=1}^n c_{kp}m_{2i-1,2p-1}\right)\left(\sum_{q=1}^n c_{kq}m_{2i,2q-1}\right)\right] = 0 \tag{129}$$

$$(2i,2i) \;:\; -4\xi_i\omega_i m_{2i,2i} - 2\omega_i m_{2i-1,2i} - \frac{1}{\mathrm{v}}\sum_{k=1}^r\left(\sum_{p=1}^n c_{kp}m_{2i,2p-1}\right)^2 + \omega_i^2\mathrm{w}\sum_{k=1}^l b_{i1}^2 = 0 \tag{130}$$

$$(2i-1,2j-1) \;:\; \omega_i m_{2i,2j-1} + \omega_j m_{2i-1,2j} - \frac{1}{\mathrm{v}}\sum_{k=1}^r\left[\left(\sum_{p=1}^n c_{kp}m_{2i-1,2p-1}\right)\left(\sum_{q=1}^n c_{kq}m_{2j-1,2q-1}\right)\right] = 0 \tag{131}$$

$$(2i-1,2j) \;:\; -2\xi_j\omega_j m_{2i-1,j} + \omega_i m_{2i,2j} - \omega_j m_{2i-1,2j-1} - \frac{1}{\mathrm{v}}\sum_{k=1}^r\left[\left(\sum_{p=1}^n c_{kp}m_{2i-1,2p-1}\right)\left(\sum_{q=1}^n c_{kq}m_{2j,2q-1}\right)\right] = 0 \tag{132}$$

$$(2i,2j-1) \;:\; -2\xi_i\omega_i m_{2i,2j-1} - \omega_i m_{2i-1,2j-1} + \omega_j m_{2i,2j}$$

$$-\frac{1}{\mathrm{v}}\sum_{k=1}^{r}\left[\left(\sum_{p=1}^{n}c_{kp}m_{2i,2p-1}\right)\left(\sum_{q=1}^{n}c_{kq}m_{2j-1,2q-1}\right)\right]=0 \tag{133}$$

$$(2i,2j) \quad : \quad -2(\xi_i\omega_i+\xi_j\omega_j)m_{2i,2j}-\omega_i m_{2i-1,2j}-\omega_j m_{2i,2j-1}$$
$$-\frac{1}{\mathrm{v}}\sum_{k=1}^{r}\left[\left(\sum_{p=1}^{n}c_{kp}m_{2i,2p-1}\right)\left(\sum_{q=1}^{n}c_{kq}m_{2j,2q-1}\right)\right]+\omega_i\omega_j\mathrm{w}\left(\sum_{k=1}^{l}b_{ik}b_{jk}\right)=0 \tag{134}$$

It is no longer possible to obtain a minimum bound on the $m_{2i-1,2i}$ terms due to the appearance of an unbounded $m_{2i,2i}$ term in the $(2i,2i)$ equations. However, since the undamped system is the limiting case as $\xi \to 0$, we know that for small enough x_i's, the diagonal terms of M will come to dominate as before.

First, notice that the bounds on off-diagonal terms from the undamped case are approximately correct for light damping. By positive-definiteness, $\forall\, i$,

$$m_{2i,2i} \geq 0 \tag{135}$$

Thus, as before from equation $(2i,2i)$,

$$m_{2i-1,2i} \geq 0 \tag{136}$$

Therefore, the bounds on the components of MC^T in (105) still hold. Now consider the coefficients of the off-diagonal terms of M that appear in the off-diagonal equation blocks (131) to (134) from $AM+MA^T$. To solve for a single term of M in order to apply bounds as was done in (111) through (114), we could invert the matrix

$$\begin{bmatrix} 0 & \omega_j & \omega_i & 0 \\ -\omega_j & -2\xi_j\omega_j & 0 & \omega_i \\ -\omega_i & 0 & -2\xi_i\omega_i & \omega_j \\ 0 & -\omega_i & \omega_j & -2(\xi_i\omega_i+\xi_j\omega_j) \end{bmatrix} \tag{137}$$

and multiply the inverse times equations (131) to (134). However, we will simply note that for $\xi_i, \xi_j \ll 1$, the inverted matrix is approximately the same as for the undamped case, $\xi_i, \xi_j = 0$, so we will take equations (111) to (114) to be approximately correct for lightly damped as well as undamped systems.

Returning to the diagonal equation blocks, from (130) and (129) and using the bounds from (105), we obtain

$$\omega_{2i-1}(m_{2i,2i}-m_{2i-1,2i-1}) = \frac{\xi_i}{\mathrm{v}}\sum_{k=1}^{r}\left(\sum_{p=1}^{n}c_{kp}m_{2i-1,2p-1}\right)^2+\frac{1}{\mathrm{v}}\sum_{k=1}^{r}\left(\sum_{p=1}^{n}c_{kp}m_{2i-1,2p-1}\right)\left(\sum_{q=1}^{n}c_{kq}m_{2i,2q-1}\right) \tag{138}$$

$$|m_{2i,2i}-m_{2i-1,2i-1}| \leq (b_i')^2\omega_i\mathrm{w}(1+\xi_i) \tag{139}$$

Now, assume $|m_{2i,2i}-m_{2i-1,2i-1}| \approx 0$ and also that diagonal terms dominate M. If true, the sum of (130) and (**??**) reduces to

$$\frac{1}{\mathrm{v}}\sum_{k=1}^{r}\left(c_{ik}m_{2i-1,2i-1}\right)^2+4\xi_i\omega_i m_{2i-1,2i=1}-\omega_i^2\mathrm{w}\sum_{p=1}^{l}b_{ip}^2\approx 0 \tag{140}$$

From the quadratic equation,

$$m_{2i-1,2i-1}\approx\frac{-4\xi_i\omega_i+\sqrt{\left(4\xi_i\omega_i\right)^2+\frac{4\omega_i^2\mathrm{w}}{\mathrm{v}}\left(\sum_{k=1}^{r}c_{ik}^2\right)\left(\omega_i^2\mathrm{w}\sum_{p=1}^{l}b_{ip}^2\right)}}{\frac{2}{\mathrm{v}}\sum_{k=1}^{r}c_ik^2} \tag{141}$$

If $m_{2i-1,2i-1}$ obtained from this equation is much larger than the bounds on the off-diagonal terms from (111) to (114) and the bound on $|m_{2i,2i}-m_{2i-1,2i-1}|$ from (138), then this approximation is valid. Furthermore, it is clear that as $\xi_i\rightarrow 0$,

$$m_{2i-1,2i-1}\rightarrow\frac{\sqrt{\sum_{p=1}^{l}b_{ip}^2}\omega_i\sqrt{\mathrm{wv}}}{\sqrt{\sum_{k=1}^{r}c_{1i}^2}} \tag{142}$$

,

same as the undamped system.

.0.4 Discrete time

Now consider a discrete time model of the system formed by the continuous system in (**??**) passed through a zero-order hold with step time $\triangle T_s$:

$$\begin{aligned} x(k+1) &= A_dx(k)+B_du(k)+B_{wd}w(k) && (143)\\ y(k) &= C_dx(k) && (144)\\ z(k) &= D_dx(k) && (145)\end{aligned}$$

Let the objective function for this system be

$$J_{H2,d}=\min_{K_d,F_d(\Phi)}E\left[\sum_{k=0}^{\infty}z(k)^Tz(k)+u(k)^TRu(k)\right] \tag{146}$$

with optimal linear controller K_d and filter F_d obtained from digital Riccati equations

$$\begin{aligned} K_d &= \left[R+B_d^TP_dB_d\right]^{-1}B_d^TP_dA_d && (147)\\ F_d &= M_dC_d^T\left[C_dM_dC_d^T+vI\right]^{-1} && (148)\\ P_d &= A_d^TP_dA_d+D_d^TD_d-A_d^TP_dB_d\left[B_d^TP_dB_d+R\right]^{-1}B_d^TP_dA_d && (149)\\ M_d &= A_dM_dA_d^T+B_{wd}wB_{wd}^T-A_dM_dC_d^T\left[C_dM_dC_d^T+vI\right]^{-1}C_dM_dA_d^T && (150)\\ & && (151)\end{aligned}$$

The objective function can be evaluated as

$$J_{H2,d} = tr\left[P_d(B_d K_d Z_d A_d^T + B_{wd} w B_{wd}^T)\right] \tag{152}$$

where Z_d is the estimation error covariance matrix

$$\begin{aligned} Z_d &= M_d - M_d C_d^T \left[C_d M_d C_d^T + vI\right]^{-1} C_d M_d & (153)\\ M_d &= A_d M_d A_d^T + B_{wd} w B_{wd}^T & (154) \end{aligned}$$

In the singular case $R \to 0$, from [12] and [13],

$$\begin{aligned} P_d &\to D_d^T D_d & (155)\\ K_d &\to (D_d B_d)^{-1} D_d A_d & (156) \end{aligned}$$

Inserting the limits of P_d and K_d in (152) and substituting for Z_d from (154) results in the same summation of M_d and D_d terms as for the continuous time case

$$\begin{aligned} J_{H2,d} &= tr\left[D_d^T D_d B_d (D_d B_d)^{-1} D_d A_d Z_d A_d^T + D_d^T D_d B_{wd} w B_{wd}^T\right] & (157)\\ &= tr\left[D_d^T D_d (A_d Z_d A_d^T + B_{wd} w B_{wd}^T)\right] & (158)\\ &= tr\left[D_d^T D_d M_d\right] & (159)\\ &= \sum_i \sum_j m_{2i-1,2j-1} d_i d_j & (160) \end{aligned}$$

Futhermore, the continuous time solution of the Riccati equation is the limiting case of the discrete Riccati equation when $\triangle T_s \to 0$. When the sampling frequency is high relative to the natural frequencies of the modes,

$$M_d \to M \triangle T_s \tag{161}$$

Therefore, M_d is proportional to the continuous M for small step times, in which case the approximations described previously may be used to obtain optimal sensor locations.